34

Characterization of Ceramic Materials Synthesized by Mechanosynthesis for Energy Applications

Claudia A. Cortés-Escobedo[1], Félix Sánchez-De Jesús[2,*], Gabriel Torres-Villaseñor[3], Juan Muñoz-Saldaña[4] and Ana M. Bolarín-Miró[2]
[1]*Centro de Investigación e Innovación Tecnológica del IPN,*
[2]*Universidad Autónoma del Estado de Hidalgo-AACTyM,*
[3]*Instituto de Investigaciones en Materiales-UNAM,*
[4]*Centro de Investigación y Estudios Avanzados del IPN, Unidad Querétaro, México*

1. Introduction

The close relationship between processing, structure and properties of materials is well known. Some of the most useful tools to elucidate the best choice in processing for a given application are scanning electron microscopy (SEM), transmission electron microscopy (TEM), scanning transmission electron microscopy (STEM), selected area electron diffraction (SAED) and x-ray diffraction (XRD). In this chapter we will focus on the application of these techniques to the characterization of ceramic materials processed by mechanosynthesis, evaluating the effect of the milling process on their physical properties.

The ceramics that are the focus of this chapter, lanthanum manganites, have a Perovskite-structure (ABO_3), with the general chemical formula $R_{1-x}A_xMnO_3$ (where R^{3+} = La, and A^{2+} = Ca and Sr). Perovskite structures have been extensively studied for almost 50 years (Coey & Viret, 1999). Since the initial discovery of their electrical and magnetic properties, the interest in these compounds has remained high, and they have been the focus of significant scientific activity throughout the past decade. This kind of ceramic material has a wide variety of applications due to its ionic conduction, magnetic, thermal and mechanical properties, etc. Furthermore, it is known that the physical properties of Perovskite manganites depend on many factors, such as external pressure (Hwang & Palstra, 1995; Neumeier et al., 1995), magnetic field (Asamitsu et al., 1995; Kuwahara et al., 1995), structure (Tokura et al., 1994) and chemical composition (Hwang et al., 1995; Mahesh et al., 1995; Schiffer et al., 1995). For example, the ionic conduction of lanthanum manganates has led to their use in oxygen sensors and solid oxide fuel cells (Shu et al., 2009). Their ionic conduction is due to punctual defects, in the form of oxygen vacancies, in the crystalline structure of the Perovskite lattice. The generation of punctual defects is activated by the addition of doping atoms, as well as changing synthesis precursors and by applying mechanical energy, all of which are typical processes going on during the high-energy ball-milling process. These effects are described in detail in this chapter.

* Corresponding Author

There are several methods to synthesize lanthanum manganites. The traditional method is via solid-state reaction of the components (mixed oxides route). Controlling the temperature during the solid state reaction is the major challenge to obtaining homogeneity in the stoichiometry, grain size, porosity and purity. Alternatively, chemical methods such as sol-gel (Zhou et al., 2010), solution combustion (Shinde et al., 2010), co-precipitation (Uskokovic & Drofenik, 2007), and others (Jafari et al., 2010) have been used, resulting in lanthanum manganites with a wide variety of physical properties.

Another technique, high-energy ball-milling, used to promote mechanosynthesis of nanostructured manganites, such as $La_{1-x}Ca_xMnO_3$, by mechanical activation of chloride and oxide compounds, has shown excellent results (Muroi et al., 2000; Bolarín et al., 2006, 2007). Zhang et al. (Zhang & Saito, 2000, Zhang et al., 2000) synthesized $LaMnO_3$ Perovskites at room temperature by milling a mixture of Mn_2O_3 and La_2O_3 powders using a planetary ball mill. Additionally, K. Sato et al. (Sato et al., 2006) used an alternative mechanical synthesis route to produce fine $LaMnO_3$ powder – compression and shear stress were repeatedly applied to a mixture of La_2O_3 and Mn_3O_4 using an attrition type milling apparatus.

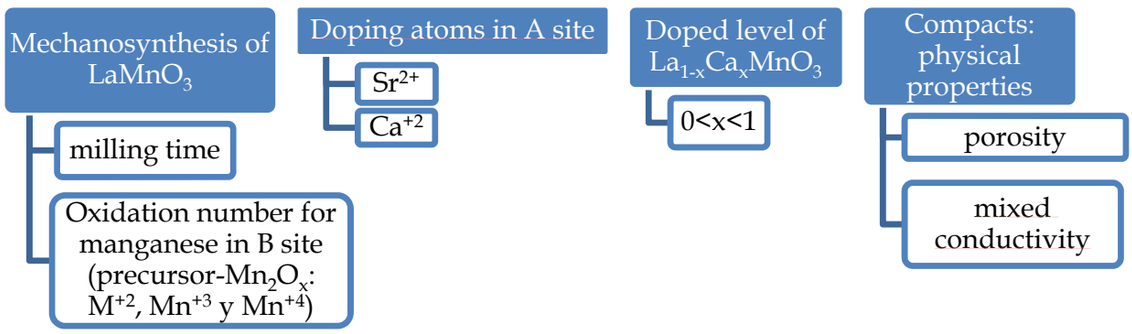

Fig. 1. Variables used to maximize punctual defects, and therefore ionic conduction in doped lanthanum manganites.

The chapter is divided in four main parts. In the first, details of the mechanosynthesis of lanthanum manganites, showing the process parameters that are necessary to carry out the synthesis of this ceramic material without a posterior annealing treatment are presented. The effect of these process parameters on the crystalline structure of the Perovskite-type manganites and mixed ionic-electronic conductivity will be presented and discussed (Figure 1). Specifically, the synthesis of lanthanum manganese oxide ($LaMnO_3$) by solid-state reaction using high-energy reactive ball milling from manganese oxides (MnO, Mn_2O_3, MnO_2) mixed with lanthanum oxide in stoichiometric ratios, for different milling times is reported. This is a useful route used to maximize punctual defects while preserving the initial structure by using manganese oxides with different oxidation numbers for manganese (Mn^{2+}, Mn^{3+} and Mn^{4+}). The mechanical energy of the mechanosynthesis processs induces a higher level of intrinsic defects than can be created by other synthesis methods (Cortés-Escobedo et al., 2008). In addition, a comparative study of mechanosynthesis with the solid-state reaction at high temperature is presented. In this section, we demonstrate the usefulness of electronic microscopy and x-ray diffraction to provide a structural description of the synthesized material.

In the second part of the chapter, the effects of doping on the structure and physical properties of lanthanum manganite is emphasized, using Ca^{+2} and Sr^{+2} as doping atoms in

A-sites of the Perovskite structure. Results of crystal structure analyses of calcium-doped lanthanum manganites, $La_{1-x}Ca_xMnO_3$ have been previously reported. The calcium-to-lanthanum ratio *x* was varied from 0 to 1 in increments of 0.1, allowing the study of changes in crystal structure with different degrees of calcium substitution, from $LaMnO_3$ (x=0) to $CaMnO_3$ (x=1) (Lira-Hernández et al., 2010). Here we present a study to increase the calcium content while maintaining the orthorhombic in order to obtain the best ion-electronic conduction. The repercussions of the doping on the microstructural characteristics were studied by means of XRD and TEM /SAED.

The third part of the chapter is dedicated to the process of consolidating manganite powder in order to see how the compaction and sintering process affects the physical properties of the ceramic. A study of the relationship between the crystalline structure, the mixed ionic-electronic conductivity and calcium content in calcium-doped lanthanum manganites, $La_{1-x}Ca_xMnO_3$, is presented.

Finally, in the fourth part of the chapter, the interaction between lanthanum manganites and yttria-stabilized zirconia, which are used as cathode and electrolyte, respectively, in both solid oxide fuel cells and sensors is discussed. A reduction in ionic conductivity is observed at certain temperatures, due to the formation of a very stable pyrochlore phase (lanthanum zirconate). Diffusion from manganite to zirconia to form zirconate has been well demonstrated by backscattered electron microscopy, showing the microstructure of cubic zirconia, in contrast with tetragonal zirconia, lanthanum manganite and lanthanum zirconate.

2. Theoretical aspects of mechanochemical processing (MCP)

Mechanochemical processing (MCP), or mechanosynthesis, is a synthesis method that uses mechanical energy (e.g., ball milling) to activate chemical reactions and structural changes in powder mixtures. In some cases, milling is followed by a low-temperature heat treatment to complete the reaction. In this study, lanthanum manganites were produced from oxide precursors La_2O_3, Mn_2O_x and CaO or SrO by means of high-energy ball millling, with a subsequent heat treatment.

Lanthanum manganites, $La_{1-x}M_xMnO_3$ ($0 < x < 1$), where M was Ca^{+2} or Sr^{+2}, were prepared using a SPEX 8000 D high-energy ball mill. Powders of Mn_2O_x and La_2O_3 were mixed in stoichiometric proportion for obtaining different level of doped manganite. MCP was carried out at room temperature in air atmosphere, in hardened-steel vials with steel balls as milling elements; ball-to-powder weight ratio was 10:1 at different milling times. X-ray diffraction (XRD) was used to evaluate phase transformations as function of milling time. Morphology and particle size of the manganites were characterized by scanning electron microscopy (SEM). Particle size distribution was measured by a zeta size analyzer. Selected area electron diffraction (SAED) patterns, obtained using a transmission electron microscope, were indexed to identify the resultant crystalline phase. Rietveld refinements of the XRD patterns were performed with the purpose of identifying and quantifying the phases and to identify the structural changes in the starting oxides until the formation of manganites.

For applications as sensors, as well as cathodes in solid oxide fuel cells, ionic conductivity of lanthanum manganites is desired. However, ionic conductivity is favored by punctual

defects in the structure of the Perovskite ceramic. For magnetic applications, it has been discussed that punctual defects have an effect on the colossal magnetoresistance of the material. For these reasons, punctual defects were induced, firstly by changing the oxidation number of manganese in precursor manganese oxide in Mn^{+2}, Mn^{+3} and Mn^{+4}, it is to say, by inducing intrinsic defects and secondly by inserting calcium or strontium atoms which will suit in A sites (in place of lanthanum), inducing extrinsic defects in the atomic structure.

3. Defects in ceramic materials

In general, properties of solid ionics and in particular ceramic materials depend on crystalline structure and chemical bonding, and sometimes these properties can be improved by means of the processing or synthesis route employed. One of the ways to improve mechanical, electrical, magnetic, and structural properties is by inducing defects in crystalline structure. Defects are deviations from ideality in crystals and can be volumetric (3-dimensional), surface (2-dimensional), or punctual (1-dimensional). Punctual defects in ionic solids can be intrinsic, this is, due to disorder in atomic arrangement. Cations may be shifted to interstitial sites (Frenkel defect) or there may be a lack of an anion-cation pair (Schottky defect), both cases leading to a vacancy. Punctual defects can also be extrinsic, due to a substitution of an atom with another that has a different size and shell configuration, resulting in vacancy generation to maintain electroneutrality. The presence of intrinsic or extrinsic defects in ceramics promotes mobility of ions driven by local electrical charges present in vacancies, improving ionic conduction properties.

3.1 Intrinsic defects in ceramic materials

Intrinsic defects can be promoted by different synthesis or processing routes. One way to promote intrinsic defects is synthesizing by mechanical milling. This process generates nanometric-sized particles and disorder at the atomic level. It is important to consider that vacancies in the crystalline structure can also be induced by using precursors composed of cations with non-stoichiometric oxidation numbers.

With the intention of promoting intrinsic defects, a stoichiometric mixture of MnO and La_2O_3 were milled to follow the reaction:

$$La_2O_3 + 2MnO \xrightarrow{MCP} 2LaMnO_3 + 2Mn'_{Mn} + 2V_O^{\cdot} \quad (1)$$

After 630 min of milling, the x-ray diffraction pattern (Figure 2) reveals the amorphization of the precursor mixture. But after 600 min of heat treatment at 1000°C, orthorhombic $LaMnO_3$ is formed. This can be represented by the following reaction:

$$0.5La_2O_3 + MnO + 0.5O_2 \xrightarrow{MCP/630\,\text{min}} (0.5La_2O_3 + MnO)_{fine-grained} + 0.5O_2 \xrightarrow{1000°C/600\,\text{min}} LaMnO_3 \quad (2)$$

A stoichiometric mixture of precursors Mn_2O_3 and La_2O_3 were milled from 0 to 540 min, and x-ray diffraction patterns are shown in Figure 3. Formation of lanthanum manganite can be detected after 60 min, and the precursors were completely consumed after 210 min of milling, following the reaction:

$$0.5La_2O_3 + 0.5Mn_2O_3 \xrightarrow{MCP/30\,\text{min}} (La_2O_3 + Mn_2O_3)_{fine\ grained}$$
$$\xrightarrow{MCP/60\,\text{min}} LaMnO_3 + (La_2O_3 + Mn_2O_3)^{remnant}_{fine\ grained} \quad (3)$$
$$LaMnO_3 + (La_2O_3 + Mn_2O_3)^{remnant}_{fine\ grained} \xrightarrow{MCP/210\,\text{min}} LaMnO_3$$

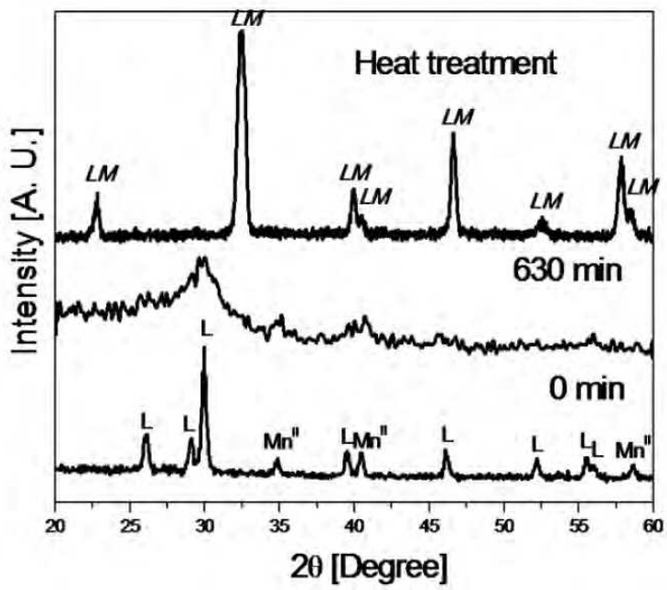

Fig. 2. X-ray diffraction patterns obtained from La_2O_3 + MnO powder mixtures before milling, milled for 630 min, and heat treated at 1000°C for 600 min (L: La_2O_3, JCPDS No. 05-0602; M^{II}: MnO, JCPDS No. 07-0230; LM: $La_{1-x}Mn_{1-z}O_3$). The pattern for Mn^{II}+L milled for 630 min was rescaled for easier comparison (Cortés-Escobedo et al., 2007).

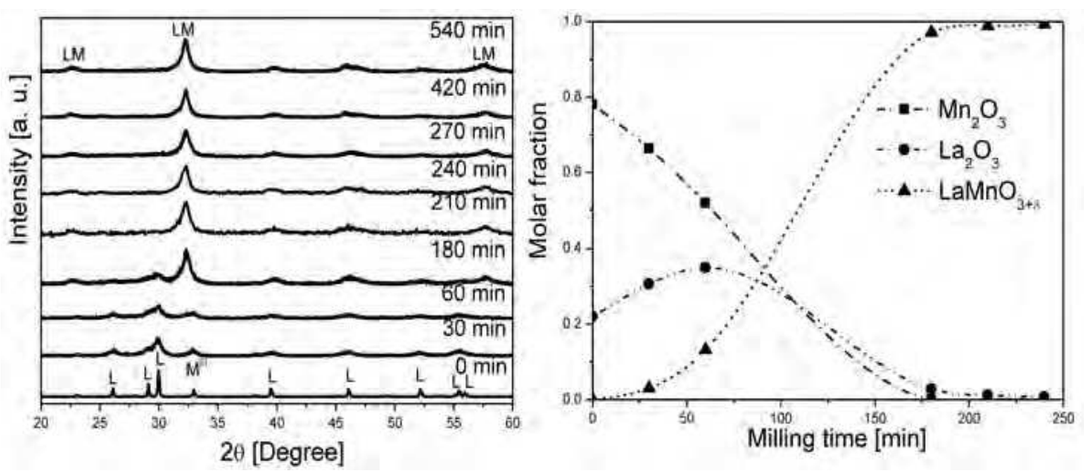

Fig. 3. Left: X-ray diffraction patterns obtained from a mixture of La_2O_3 and Mn_2O_3 powder for various milling times (M^{III}: Mn_2O_3, JCPDS No. 24-0508). Right: mol fraction of phases as analyzed using Rietveld refinement of the x-ray diffraction patterns. LM corresponds to the lanthanum manganite phases irrespective of the structure (Cortés-Escobedo et al., 2007).

Figure 4 shows the electron diffraction patterns for lanthanum manganite obtained from its stoichiometric precursors, and the rings correspond to reflections from the orthorhombic and rhombohedral structure of lanthanum manganite.

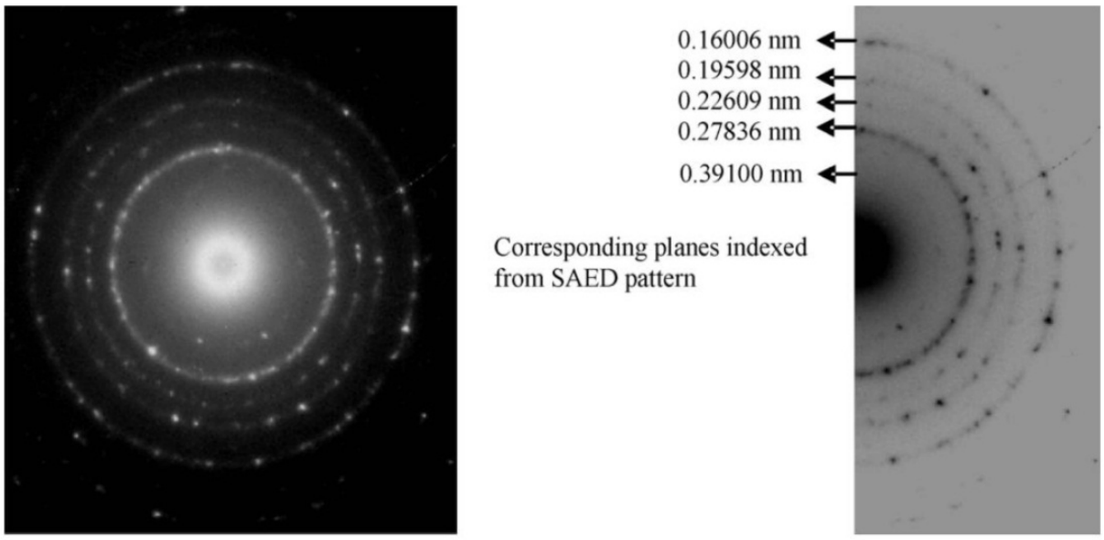

Fig. 4. Electron diffraction patterns of $LaMnO_3$ milled for 7 h, with the measured interplanar spacings (d) noted (Bolarín et al., 2007).

Finally, milling was performed using a mixture according to the following reaction:

$$La_2O_3 + 2MnO_2 \xrightarrow{MCP} 2LaMnO_3 + \frac{1}{2}O_2 + 2Mn_{Mn}^{\cdot} + V_O^x \tag{4}$$

After 270 of milling time $LaMnO_3$ is completely formed following the steps:

$$\begin{aligned} 0.5La_2O_3 + MnO_2 &\xrightarrow{MCP/90\,\text{min}} (La_2O_3 + MnO_2)_{fine\ grained} \xrightarrow{MCP/120\,\text{min}} (La_2O_3 + MnO_2)_{fine\ grained} \\ +(LaMnO_3)_{fine\ grained} &\xrightarrow{MCP/270\,\text{min}} LaMnO_3 \end{aligned} \tag{5}$$

The corresponding x-ray diffraction patterns are shown in Figure 5. After Rietveld refinement, three different structures of lanthanum manganite were identified: orthorhombic, rhombohedral and cubic, in varying proportions.

A discussion of the structures can be read in (Cortés-Escobedo et al., 2008). The particle size and morphology of the milled powders as a function of time and precursor is shown in Figure 6. The decrease in particle size as a function of time is consistent with the diminishing crystallite size observed with x-ray diffraction (Figures 3-5).

Figure 7 shows the particle size as measured by laser diffraction and image analysis of the SEM photomicrographs. In both cases, after 100 min of milling time particles of 500 nm are predominant.

In Figure 8 photomicrographs of the crystallite size for the La_2O_3+Mn_2O_3 mixture milled for 90 min show crystallites from 5 to 20 nm in size and the deformation of the particles.

Thermodynamic calculations for ΔG and ΔH were made using HSC Chemistry 5.11[2] software (Figure 9) in order to know the feasibility of the formation of $LaMnO_3$ in the three cases, and the reaction with lowest ΔG was $MnO_2 + La_2O_3 = LaMnO_3$, opposite to what was observed for the complete formation of the manganite in the milling time experiments. This difference can be attributed to structural and redox transformations required to obtain the final Perovskite structure.

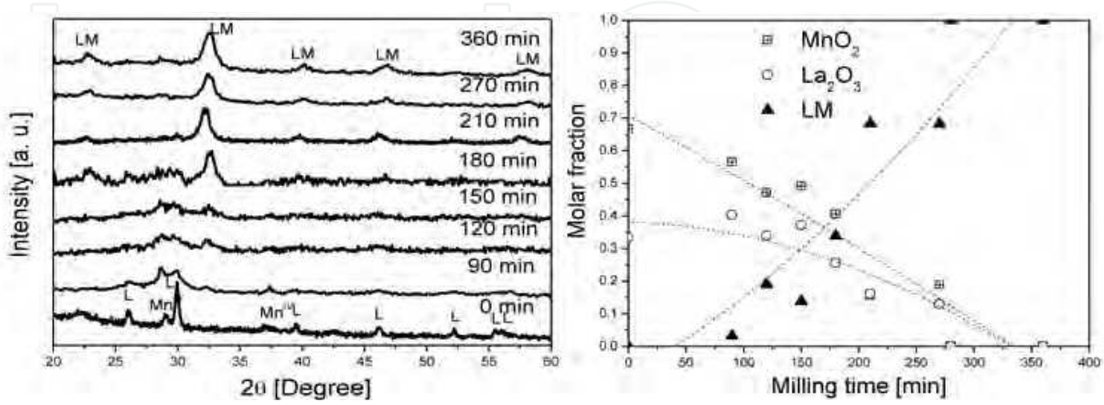

Fig. 5. Left: X-ray diffraction patterns obtained from a La_2O_3+MnO_2 powder mixture at different milling times (M^{IV}: MnO_2, JCPDS No.72-1984). Right: mol fraction of phases as analysed by the Rietveld x-ray diffraction pattern refinement, LM corresponds to the lanthanum manganite phases irrespective to the structure. (Cortés-Escobedo et al., 2007)

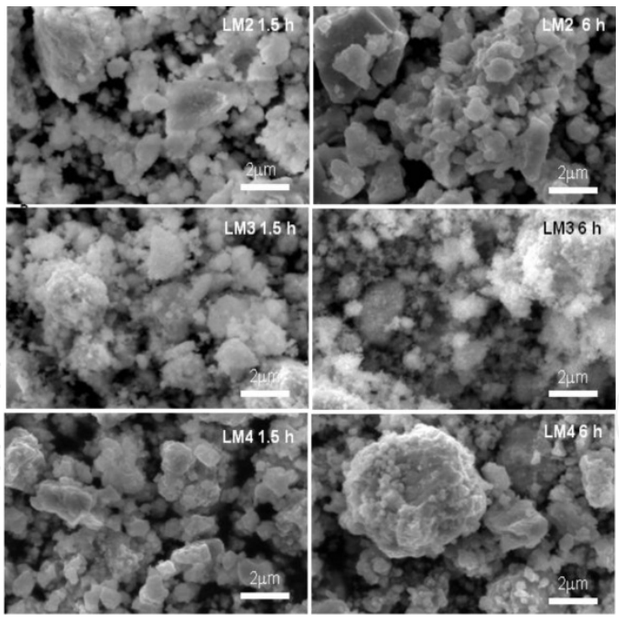

Fig. 6. Typical SEM micrographs of powder mixtures from different Mn precursors and milling times: LM2 1.5 h: La_2O_3+MnO for 90 min; LM2 6 h: La_2O_3+MnO for 360 min; LM3 1.5 h: La_2O_3+Mn_2O_3 at 90 min; LM3 6 h: La_2O_3+Mn_2O_3 at 360 min; LM4 1.5 h: La_2O_3+MnO_2 at 90 min; LM4 6 h: La_2O_3+MnO_2 at 360 min. (Cortés-Escobedo et al., 2007).

[2] HSC Chemistry 5.11, Copyright (C) Outokumpu Research Oy, Pori, Finland, A. Roine.

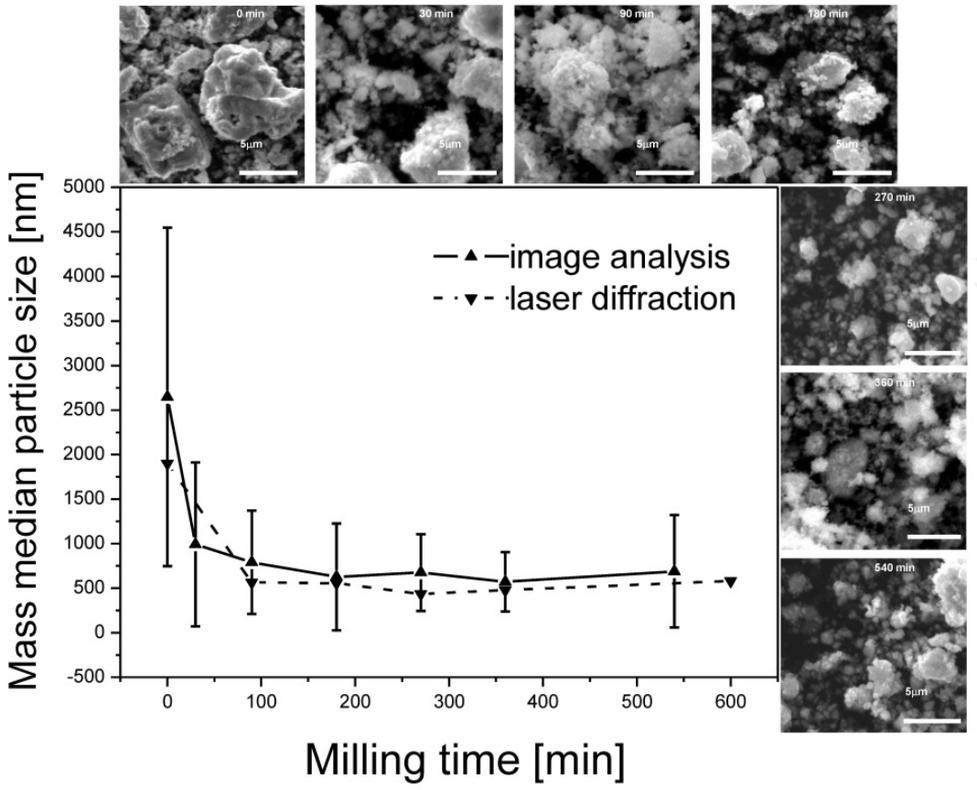

Fig. 7. Particle size results from Zetasizer measurements and image analysis of La_2O_3+Mn_2O_3 milled powders at different milling times (Cortés-Escobedo et al., 2008).

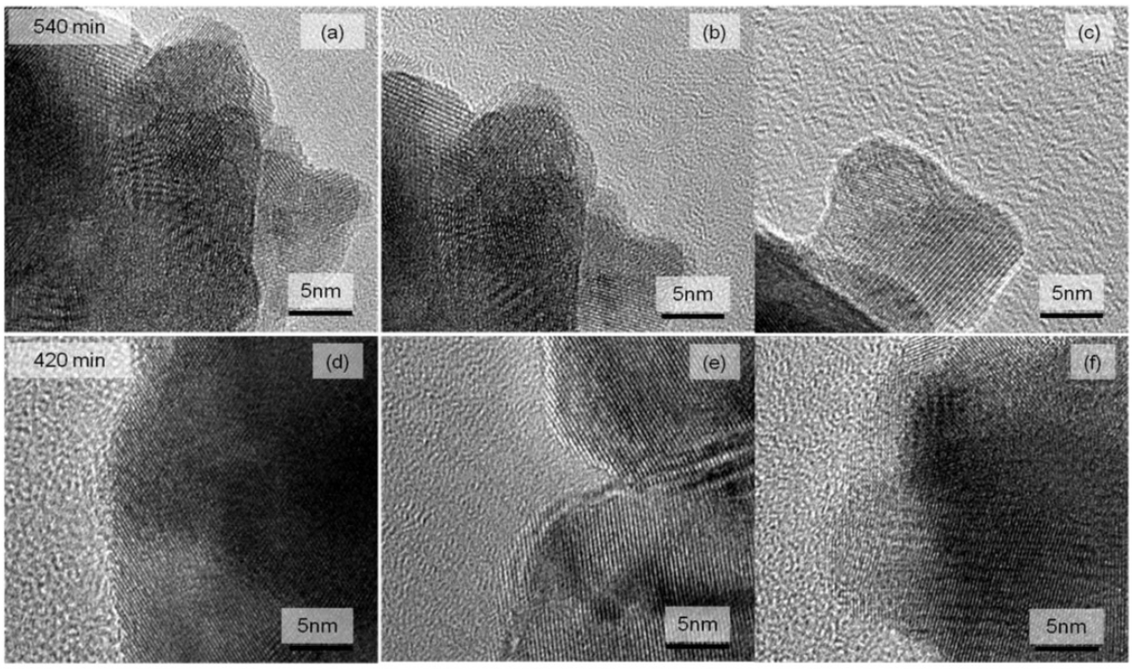

Fig. 8. HRTEM photomicrographs of the La_2O_3+Mn_2O_3 mixture milled for 540 and 420 min.

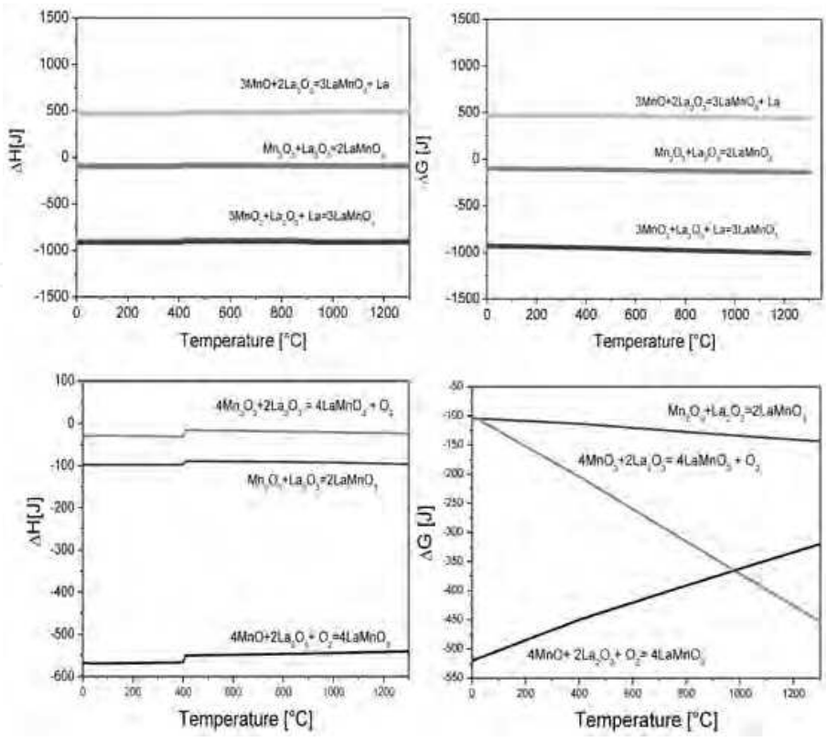

Fig. 9. Thermodynamic calculations for the reaction of formation of $LaMnO_3$ with different precursor oxides.

3.2 Extrinsic defects: Doped effect

The other way used to promote ionic conductivity was to introduce a different cation in the place of lanthanum. The cations chosen for their ionic radiuses were Ca^{2+} and Sr^{2+} (see Table 1). In the case of Ca^{2+}, the reaction expected was:

$$2La_2O_3 + 2Mn_2O_3 \xrightarrow{CaO} 2LaMnO_3 + 2Ca'_{La} + V_O^{xx} \tag{6}$$

Ion	Ionic radius (Å)
La+	1.39
La3+	1.06
Sr2+	1.12
Ca2+	0.99

Table 1. Ionic radius for different cations

Figure 10 shows x-ray diffraction patterns for $CaO+Mn_2O_3+La_2O_3$ powder mixtures milled for 7 h, with different doping levels ($0 \leq x \leq 1$). The milled precursors react according to the following expression:

$$\frac{(1-x)}{2}La_2O_3 + \frac{1}{2}Mn_2O_3 + xCaO - \frac{x}{4}O_2 \xrightarrow{MCP} La_{1-x}Ca_xMnO_3 \tag{7}$$

After 7 h of milling, there is a shift to the right of the mean peak of the lanthanum manganite as the amount of doping is increased, indicating a decrease in the interplanar distance, corresponding to deformation of the network as proposed in Figure 11.

In Figures 12- 14, morphology of the oxide precursors is shown. In the micrographs particle sizes of up to 20 μm before milling can be observed.

After 4.5 h of milling, particle sizes have decreased to around 1 μm with aggregates. Figures 15 and 16 show the aggregates and particles after 4.5 and 7 h of milling, respectively, for the stoichiometric mixture used to form $LaMnO_3$.

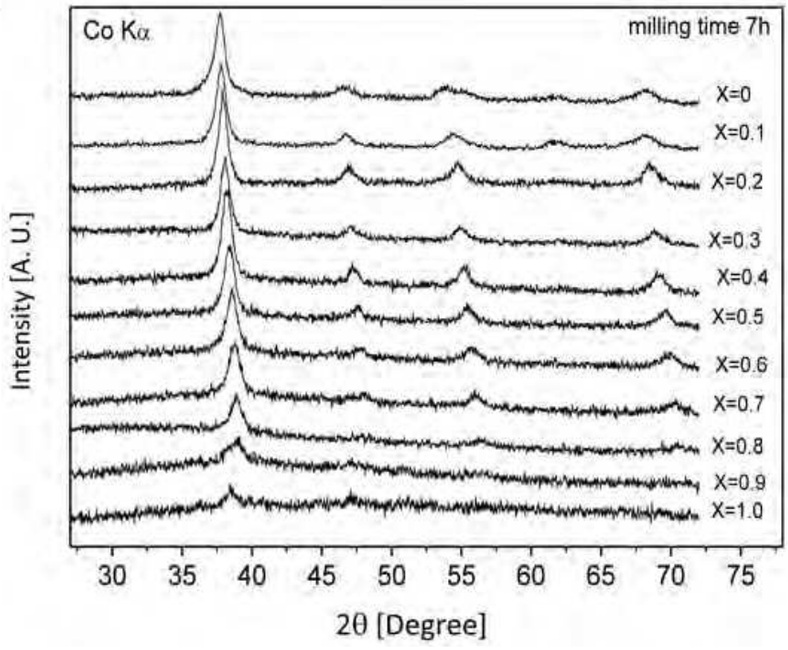

Fig. 10. X-ray powder diffraction patterns of different mixtures milled at 7 h, modifying the level of doping from x = 0 to x = 1 (Lira-Hernández et al., 2010).

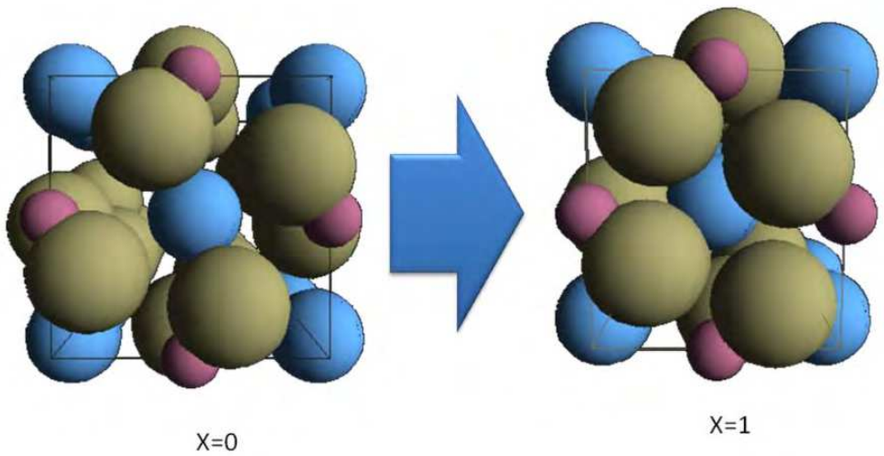

Fig. 11. Distortion of the $La_{(1-x)}Ca_xMnO_3$ unit cell.

Figures 17-19 show the morphology of the nanoparticles aggregated after 4.5 and 7 h of milling of the (Mn_2O_3+CaO+La_2O_3) mixtures. The morphology is the same for compositions x = 0.3 and 0.4, but for x = 0.8 after 7 h of milling a different morphology is observed - larger and continuous particles with softer edges.

Figure 20 shows the morphology for the extreme case of x = 1, the Mn_2O_3+CaO mixture after 4.5 h of milling, and the absence of large agglomerates is noticeable; the particle size is on the order of nanometers.

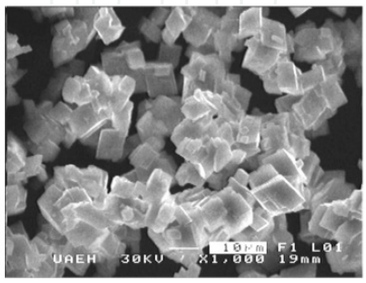

Fig. 12. Calcium oxide precursor for the reaction of formation of $La_{(1-x)}Ca_xMnO_3$.

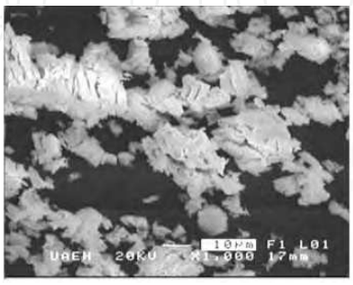

Fig. 13. Lanthanum oxide precursor for the reaction of formation of $La_{(1-x)}Ca_xMnO_3$.

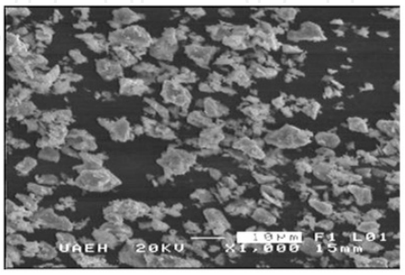

Fig. 14. Manganesum oxide precursor (Mn_2O_3) for the reaction of formation of $La_{(1-x)}Ca_xMnO_3$.

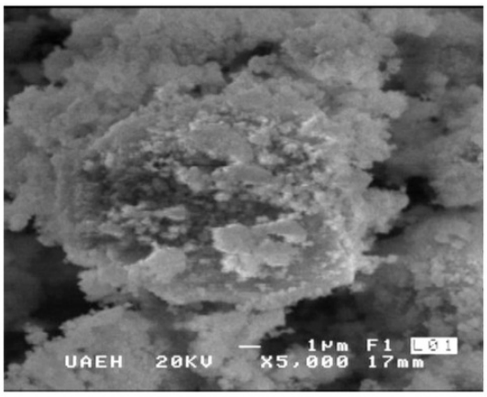

Fig. 15. (Mn_2O_3+La_2O_3) mixture after 4.5 h of milling.

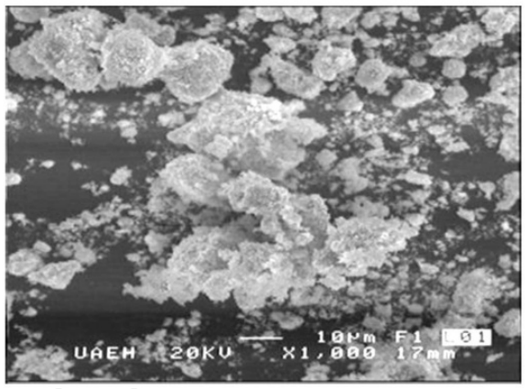

Fig. 16. (Mn_2O_3+La_2O_3) mixture after 7 h of milling.

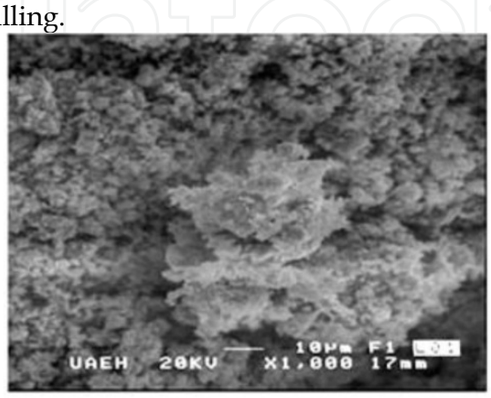

Fig. 17. (Mn_2O_3+CaO+La_2O_3) mixture after 4.5 h of milling (x = 0.3).

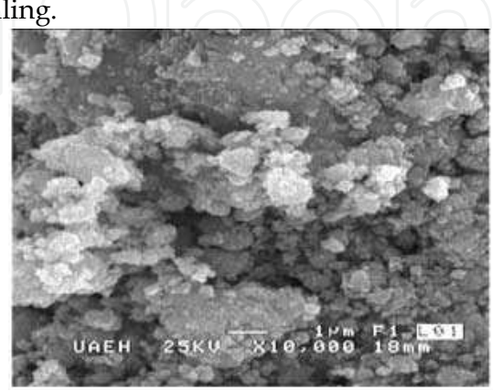

Fig. 18. (Mn_2O_3+CaO+La_2O_3) mixture after 7 h of milling (x = 0.4).

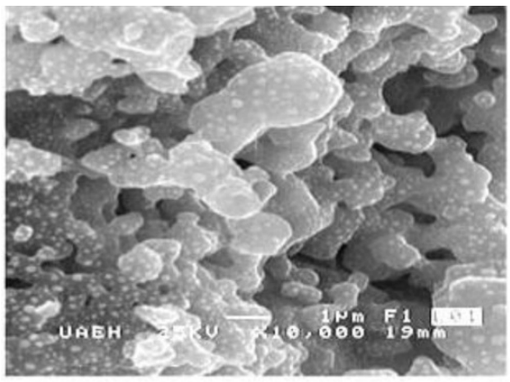

Fig. 19. (Mn2O3+CaO+La2O3) mixture after 7 h of milling (x = 0.8).

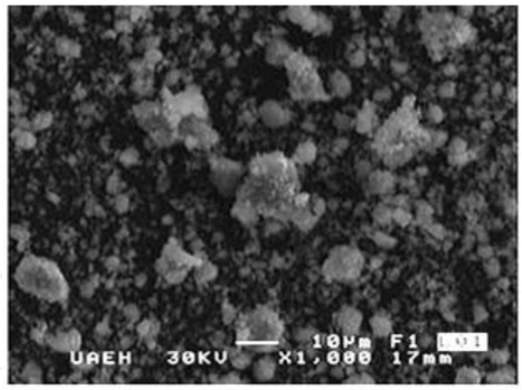

Fig. 20. (Mn2O3+CaO) mixture after 4.5 h of milling.

When substituting strontium (Sr^{2+}) for lanthanum, the expected reaction was:

$$2La_2O_3 + 2Mn_2O_3 \xrightarrow{SrO} 2LaMnO_3 + 2Sr'_{La} + V_O^{xx} \quad (8)$$

Strontium was substituted in the amounts of x = 0.15 and 0.2 according to the following reactions:

$$\frac{(1-x)}{2}La_2O_3 + MnO + xSrO + \frac{1}{4}(1-x)O_2 \xrightarrow{MCP} La_{1-x}Sr_xMnO_3 \ldots \text{LSMx2} \quad (9)$$

$$\frac{(1-x)}{2}La_2O_3 + \frac{1}{2}Mn_2O_3 + xSrO \xrightarrow{MCP} La_{1-x}Sr_xMnO_3 + \frac{(-x)}{4}O_2 \ldots \text{ LSMx3} \quad (10)$$

$$\frac{(1-x)}{2}La_2O_3 + MnO_2 + xSrO \xrightarrow{MCP} La_{1-x}Sr_xMnO_3 + \frac{(1-x)}{4}O_2 \ldots . \text{ LSMx4} \quad (11)$$

LSMx2 is shorthand for $LaMnO_3$ produced using MnO as the precursor and with *x* percent of Sr. LSMx3 is shorthand when Mn_2O_3 is the precursor, and LSMx4 is for when MnO_2 is the precursor. Thus, lanthanum manganite produced from MnO and doped with 20 at% Sr ($La_{0.8}Sr_{0.2}MnO_3$) is represented by LSM202, and lanthanum manganite produced from MnO_2 and doped with 15 at% Sr ($La_{0.85}Sr_{0.15}MnO_3$) is represented by LSM153.

The x-ray diffraction patterns for this collection of milled samples are shown in Figure 21. It is important to note that lanthanum manganites from MnO (LM2, LSM152, and LSM202) were not obtained only by MCP, but subsequently it was necessary to heat treat (1000°C for 600 min) the mixtures to produce lanthanum manganite. On the other hand, mixtures with precursors MnO_2 and Mn_2O_3 developed lanthanum manganites without heat treatment.

4. Consolidation of ceramic powders

Compaction of lanthanum manganites was carried out by using two agents, corn starch and etilen-bis-estearamide (EBS, a lubricant commonly used in powder metallurgy industry) at 200 MPa. With corn starch porosity in range from 10 to 30% was observed, and LSM204 had the largest surface area of all samples (Figure 22). Differences in morphology with different strontium contents and manganese oxide precursors were also observed. Samples of

consolidated manganites obtained from MnO had a grain size of 300-800 μm, larger than those obtained from MnO_2 (100-250 μm). Grain growth can be associated with cohesion between particles due to internal repulsi on forces which prevent recrystallization or grain growth during the sintering process.

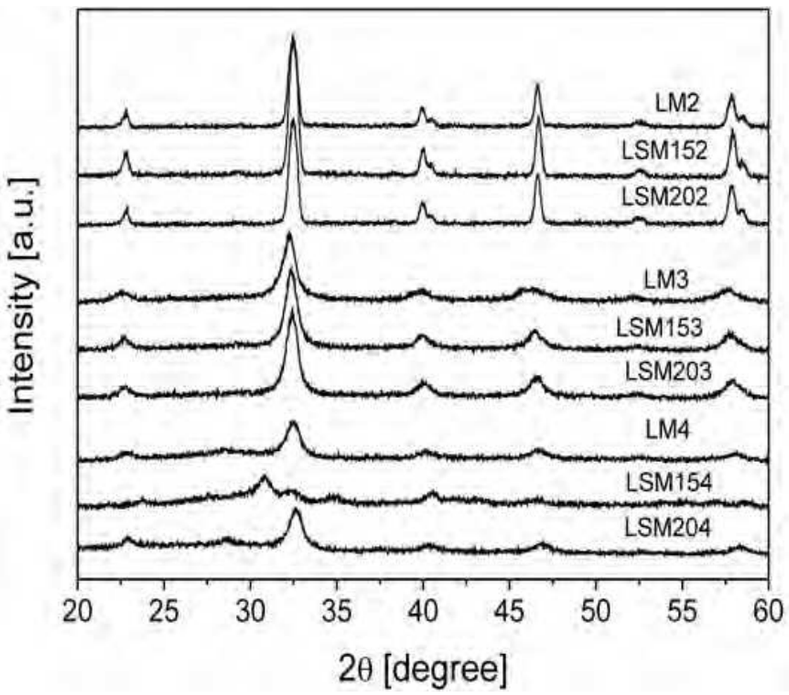

Fig. 21. X-ray diffraction patterns for the mechanosynthesis and heat treatment process (1000°C for 600 min) to obtain lanthanum manganites with intrinsic and extrinsic defects.

The microstructure is similar for pellets with 10, 15 and 20 wt% EBS (Figures 23-25). Sintering of the ceramics is indicated by necks formed after sintering at 1100°C. Heat treating at 1300°C for 3 h results in a decrease in porosity as well as particle growth.

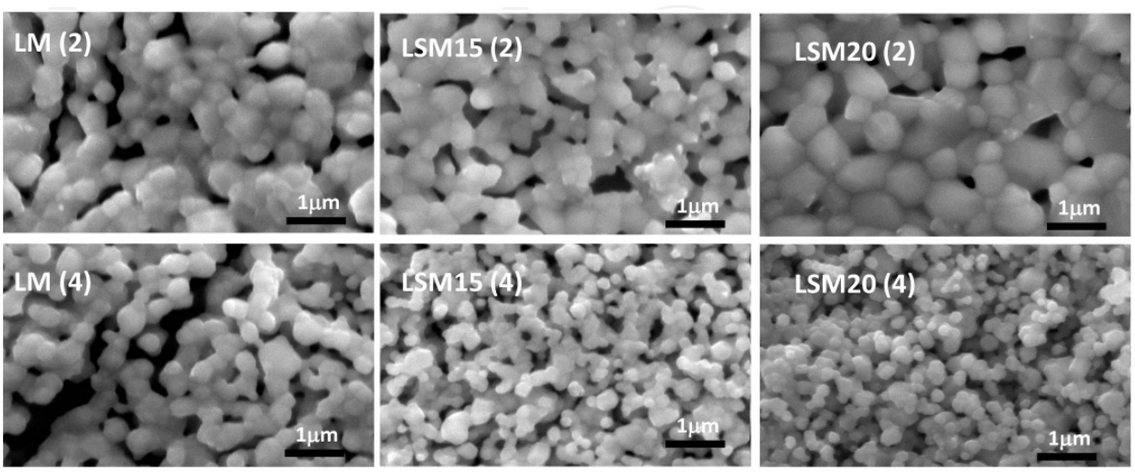

Fig. 22. SEM micrographs for lanthanum manganites consolidated with corn starch.

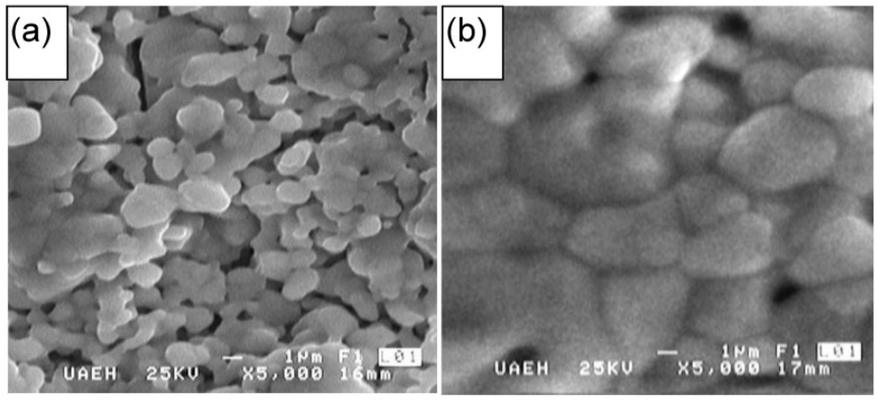

Fig. 23. SEM images of $La_{1-x}Ca_xMnO_3$ consolidated with 10 wt% EBS at: a) 1100°C for 1 h and b) 1300°C for 3 h.

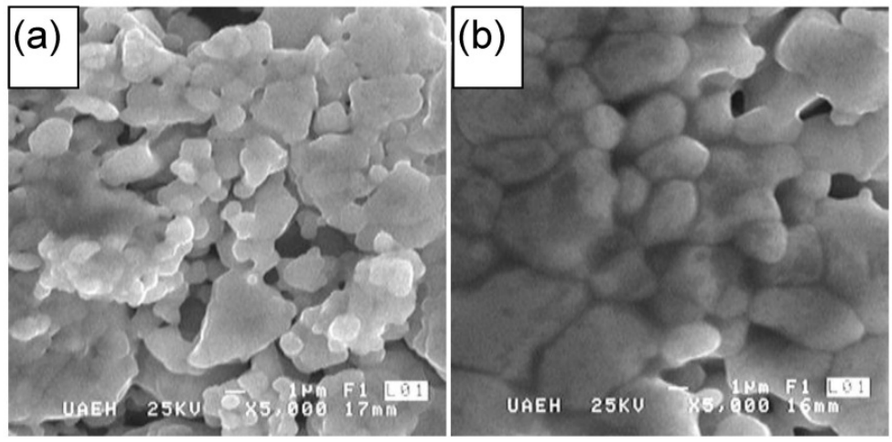

Fig. 24. SEM images of $La_{1-x}Ca_xMnO_3$ consolidated with 15 wt% EBS at: a) 1100°C for 1 h and b) 1300°C for 3 h.

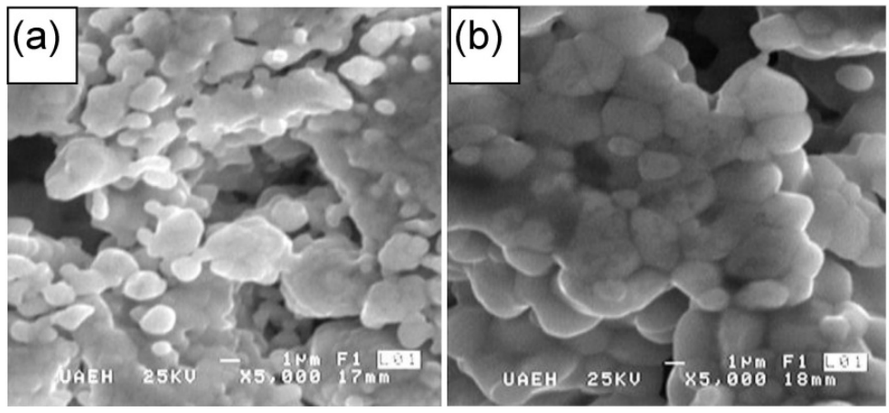

Fig. 25. SEM images of $La_{1-x}Ca_xMnO_3$ consolidated with 20 wt% EBS at: a) 1100°C for 1 h and b) 1300°C for 3 h.

5. YSZ-LSM interactions

As was mentioned previously, for applications as sensors and as cathodes in solid oxide fuel cells, the desired functionality of the material is based on the ionic conduction of oxygen through the interface between yttrium-doped zirconia (YSZ) and lanthanum manganite (LSM). This functionality can be potentiated by increasing the triple phase boundaries (TPB) formed between oxygen, YSZ and LSM (Figure 26).

But in some conditions, an undesirable reaction occurs in the TPBs, giving rise to lanthanum zirconate formation through the diffusion of lanthanum atoms from manganite to zirconia (Figure 27).

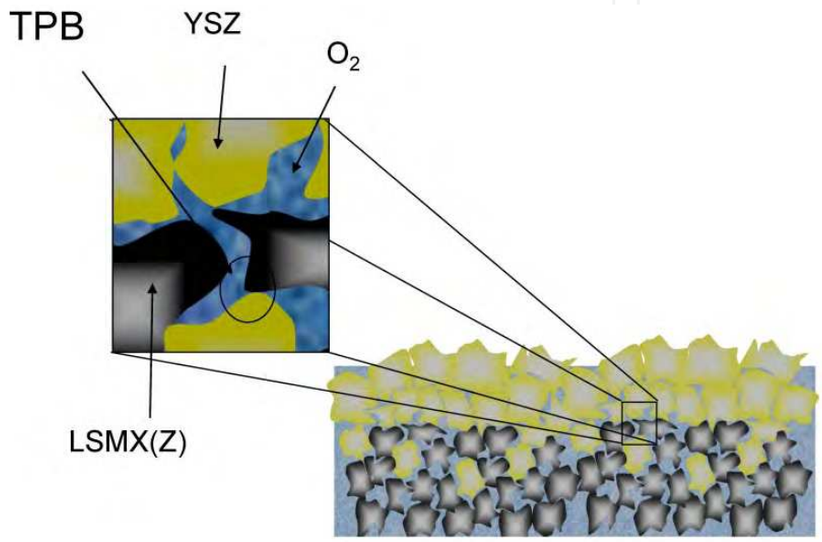

Fig. 26. Schematic of the triple phase boundaries in LSM-YSZ interfaces.

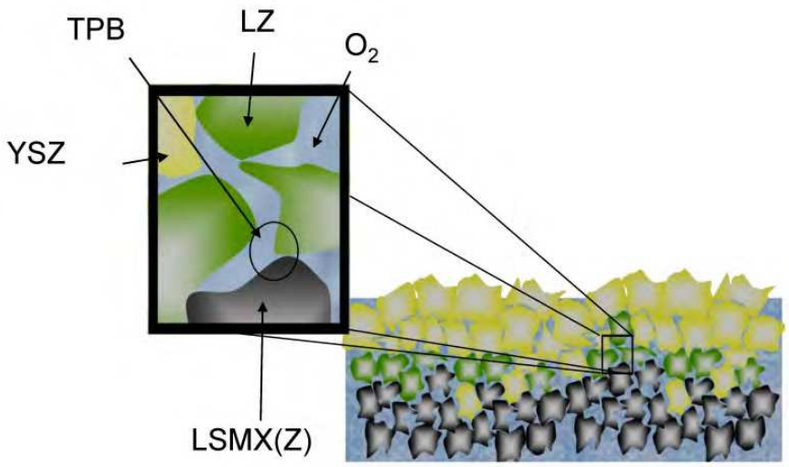

Fig. 27. Schematic of lanthanum zirconate formation in TPBs.

For this reason, it is important to determine the optimal conditions required to avoid the formation of lanthanum zirconate, which diminishes the ionic conduction through TPBs.

Heat treatment (1000 – 1300°C) and spark plasma sintering were used to obtain the conditions in which the formation of lanthanum zirconates is avoided.

Figure 28 shows the x-ray diffraction patterns of mixtures of yttria partially stabilized tetragonal zirconia (YPSZ) with lanthanum manganites synthesized from different manganese oxide precursors (LMz) without heat-treatment (Figures 28a, 28e, and 28i) and heat-treated at 1300°C (Figures 28b-28d, 28f-28h and 28j-28l).

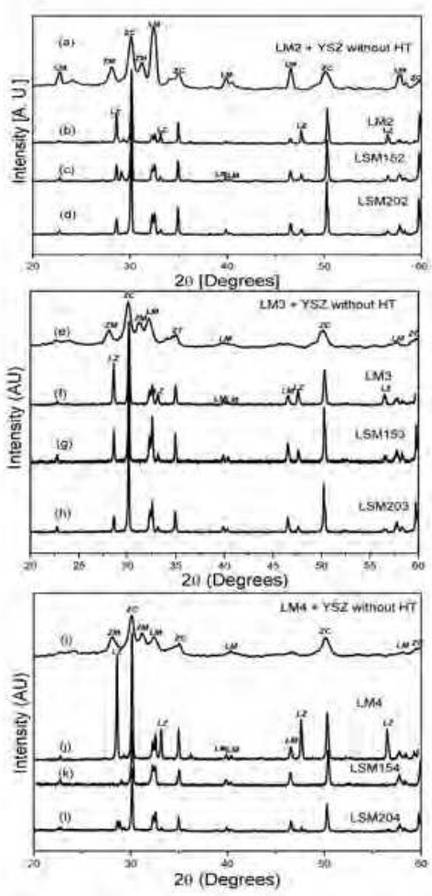

ZM = monoclinic zirconia, *ZC-T* = cubic + tetragonal zirconia, *ZT* = tetragonal zirconia, *LZ* = lanthanum zirconate, *LM* = lanthanum manganite (Cortés-Escobedo et al., 2008).

Fig. 28. X-ray diffraction patterns of mixtures of YPSZ with lanthanum manganites prepared from: (a)-(d) MnO, La_2O_3 and SrO by mechanosynthesis and heat treatment in air; (e)-(h) Mn_2O_3, La_2O_3 and SrO by mechanosynthesis; (i)-(l) MnO_2, La_2O_3 and SrO by mechanosynthesis. Manganites in mixtures (a), (b), (e), (f), (i) and (j) are undoped, while manganites in mixtures (c), (g) and (k) are doped with 15 at% Sr in La sites and (d), (h) and (l) have 20 at% Sr in La sites. All mixtures were heat-treated at 1300°C except (a), (e) and (i).

Figures 28a-b, 28e-f and 28i-j correspond to mixtures of YPSZ with undoped manganites prepared from Mn^{II}, Mn^{III} and Mn^{IV}, respectively. In these figures, increasing heat-treatment temperature is shown to result in increased intensity and a widening of the peaks (Cortés-Escobedo et al., 2008).

In all cases, grain growth is reflected in the decrease of the peak width and increase in the intensity of the peaks. The relative intensity of the main lanthanum zirconate peak is greatest for lanthanum manganite obtained from MnO_2+La_2O_3 without strontium and is smallest when doped with 15 at% strontium. In addition, there is a phase change for zirconia in the presence of lanthanum zirconate, tending to the cubic phase instead of its usual tetragonal structure (without lanthanum zirconate).

The last point can be also observed in the backscattered electron SEM micrograph (Figure 29), in which the cubic zirconia morphology (shown with small dots and in dark gray) is clearly distinguished from the lanthanum zirconate (bright gray) and the lanthanum manganite (medium gray). From this image we can also deduce the direction of the diffusion of the atoms. That is to say, lanthanum zirconate grains tend to invade zirconate grains from lanthanum manganite grains.

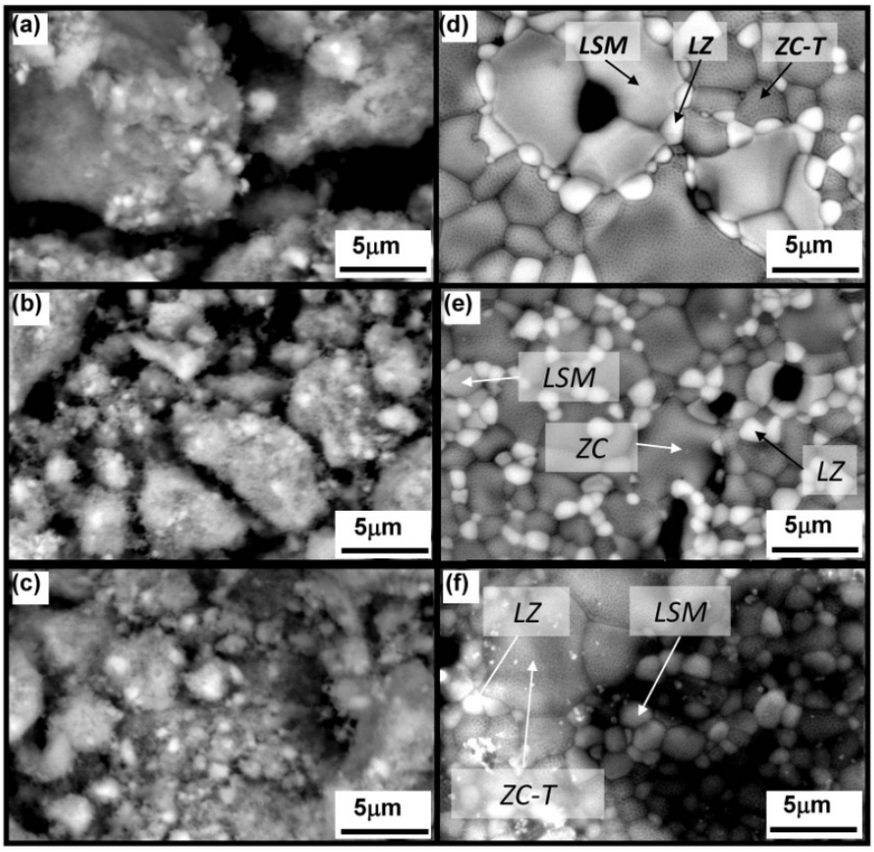

Fig. 29. SEM micrographs of the mixture of YPSZ with lanthanum manganite obtained from undoped Mn^{II} (a), (b), (c) before and (d), (e), (f) after sintering at 1300°C (Cortés-Escobedo et al., 2008). LZ: Lanthanum zirconate; LSM: Strontium doped lanthanum manganite; ZC: cubic zirconia; ZC-T: tetragonal zirconia.

In another experiment, using spark plasma sintering, for samples heat treated at 1000°C, lanthanum zirconate is observed only for sintered $LaMnO_3$ mechanosinthesized from MnO_2+La_2O_3 (LM4). But by treating at 1300°C, lanthanum zirconate is detected in all the samples (Figures 30-31).

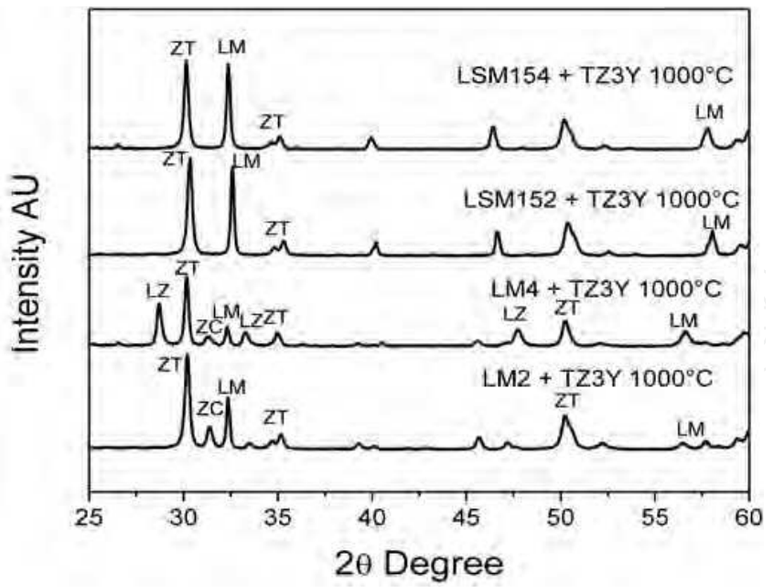

Fig. 30. X-ray diffraction of lanthanum manganite – yttria-stabilized zirconia mixtures, which have been spark plasma sintered at 1000°C for 10 min. LM2: Lanthanum manganite from MnO+La_2O_3; LM4: Lanthanum manganite from MnO_2+La_2O_3; LSM152: 15 at% Sr-doped lanthanum manganite from MnO+La_2O_3+ SrO; LSM154: 15 at% Sr-doped lanthanum manganite from MnO_2+La_2O_3+SrO.

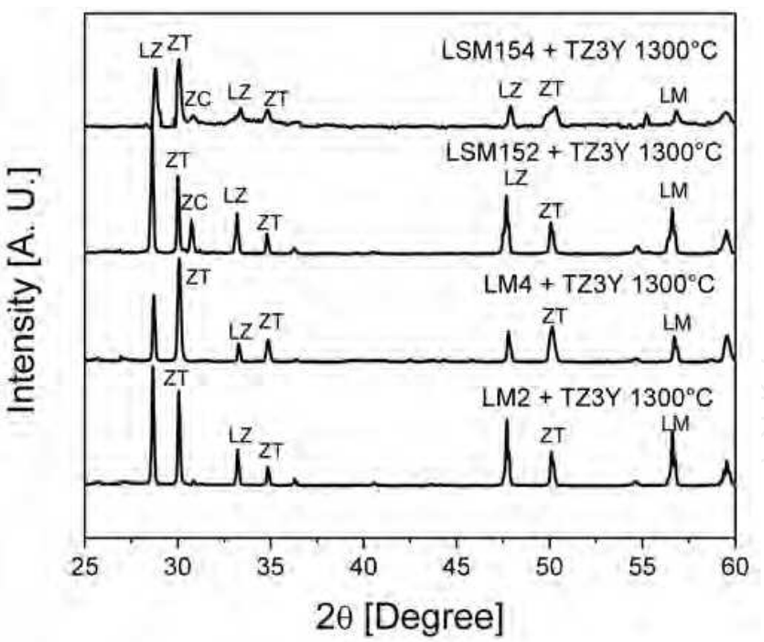

Fig. 31. X-ray diffraction of lanthanum manganite – yttria-stabilized zirconia mixtures, which have been spark plasma sintered at 1300°C for 10 min. LM2: Lanthanum manganite from MnO+La_2O_3; LM4: Lanthanum manganite from MnO_2+La_2O_3; LSM152: 15 at% Sr-doped lanthanum manganite from MnO+La_2O_3+SrO; LSM154: 15 at% Sr-doped lanthanum manganite from MnO_2+La_2O_3+SrO.

In Figure 32 SEM images show the microstructure of spark plasma sintered $LaMnO_3$ mechanosinthesized from $MnO+La_2O_3$ (LM2) and $MnO_2+La_2O_3$ (LM4) and $La_{0.85}Sr_{0.15}MnO_3$ mechanosinthesized from $MnO+SrO+La_2O_3$ (LSM152) and $MnO_2+SrO+La_2O_3$ (LSM154), treated at 1000°C and 1300°C. In the case of treatment at 1000°C, pores are present in all samples, but the differentiation between grains is diffuse. Samples treated at 1300°C show continuity in the microstructure without differentiation in grains.

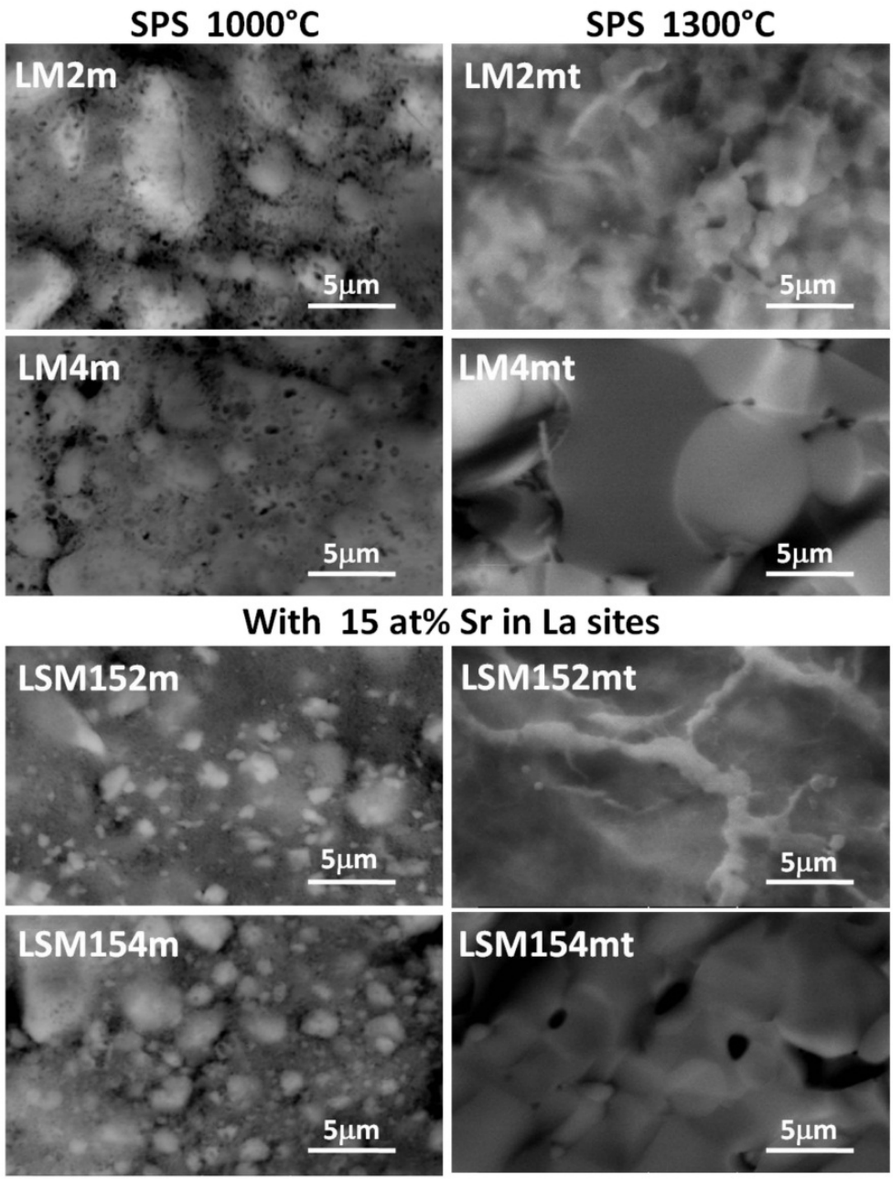

Fig. 32. SEM images of the microstructure of spark plasma sintered $LaMnO_3$ mechanosinthesized from $MnO+La_2O_3$ (LM2) and $MnO_2+La_2O_3$ (LM4) and $La_{0.85}Sr_{0.15}MnO_3$ mechanosinthesized from $MnO+SrO+La_2O_3$ (LSM152) and $MnO_2+SrO+La_2O_3$ (LSM154). On the left are samples spark plasma sintered at 1000°C, and on right are samples treated at 1300°C.

6. Acknowledgment

The results presented in this chapter were financially assisted by the Consejo Nacional de Ciencia y Tecnología, CONACyT under grants no. 157925, 129910 and 130413, and by the National Polytechnic Institute under grant no. MULT-1338 MOD-20113549. The authors thank Arturo Ponce and Adriana Tejeda Cruz, of the University of Texas at San Antonio and the Institute of Materials of UNAM, respectively, for their support in HRTEM and XRD measurements. Also, authors thank M. Boldrick (Peace Corps) for his many useful suggestions.

7. References

Asamitsu, A., Moritomo, Y., Tomioka, Y., Arima, T. & Tokura, Y. (1995). A Structural Phase Transition Induced by an External Magnetic Field. *Nature*. Vol. 373, (February 1995), pp. (407–409), ISSN 0028-0836.

Bolarín, A. M., Sánchez, F., Palomares, S., Aguilar, J.A. & Torres, G. (2007). Synthesis of calcium doped lanthanum manganite by mechanosynthesis. *Journal of Alloys and Compounds*. Vol. 436, (June 2007), pp. (335-340), ISSN 0925-8388.

Bolarín, A. M., Sánchez, F., Ponce, A. & Martinez, E. E. (2007). Mechanosynthesis of lanthanum manganite. *Materials Science and Engineering A*. Vol. 454-455, (April 2007), pp. (69-74), ISSN 0921-5093.

Coey, J.M.D. & Viret, M. (1999). Mixed Valence Manganites. *Advances in Physics*. Vol. 48 (December 1997), pp. (167-293), ISSN 1460-6976.

Cortés-Escobedo, C. A., Muñoz-Saldaña, J., Bolarín-Miró, A. M., Sánchez de Jesús, F. (2008). Determination of strontium and lanthanum zirconates in YPSZ-LSM mixtures for SOFC. *Journal of Power Sources*. Vol. 180, (May 2008), pp. (209-214), ISSN 0378-7753.

Cortés-Escobedo, C. A., Sánchez de Jesús, F., Bolarín Miró, A. M., Muñoz-Saldaña, J. (2007). Mechanosynthesis of $LaMnO_3$ from different manganese oxides. *Physica Status Solidi C*. Vol. 4, (November 2007), pp. (4054-4063), ISSN 1610-1642.

Hwang, H.Y. & Palstra, T.T.M. (1995). Pressure Effects on the Magnetoresistance in Doped Manganese Perovskites. *Physical Review B: Condensed Matter and Materials Physics*. Vol. 52, (December 1995), pp. (15046–15049), ISSN 1550-235x.

Hwang, H.Y., Cheong, S.W., Radaelli, P.G., Marezio, M., Batlogg, B. (1995). Lattice Effects on the Magnetoresistance in Doped $LaMnO_3$. *Physical Review Letters*. Vol. 75, (October 1995), pp. (914-917), ISSN 0031-9007.

Jafari-Nejad, Sh., Abolghasemi, H., Moosavian, M.A., Golzary, A. & Maragheh, M. G. (2010). Fractional factorial design for the optimization of hydrothermal synthesis of lanthanum oxide nanoparticles under supercritical water condition. *Journal of Supercritical Fluids*. Vol. 52, (April 2010), pp. (292-297), ISSN 0896-8446.

Kuwahara, H., Tomioka Y. & Asamitsu A., Moritomo, Y. & Tokura, Y. (1995). A First Order Phase Transition Induced by a Magnetic Field. *Science*. Vol. 270, (November 1995), pp. (961–963), ISSN 1095-9203.

Lira-Hernández, I. A., Sánchez-De Jesús, F., Cortés-Escobedo, C.A. & Bolarín-Miró, A.M. (2010). Crystal structure analysis of calcium doped lanthanum manganites prepared by mechanosynthesis. *Journal of the American Ceramic Society*. Vol. 93, (October 2010), pp. (3474-3477), ISSN 0002-7820.

Mahesh, R., Mahendiran, R., Raychaudhuri, A.K. & Rao, C.N.R. (1995). Effect of the Internal Pressure Due to the A-Site Cations on the Giant Magnetoresistance and Related Properties of Doped Rare-Earth Manganates $Ln_{1-x}A_xMnO_3$ (Ln = La, Nd, Gd, Y; A = Ca, Sr, Ba, Pb). *Journal of Solid State Chemistry*. Vol. 120, (November 1995), pp. (204−207), ISSN 0022-4596.

Muroi, M., Street, R. & McCormick, P.G. (2000). Structural and Magnetic Properties of Ultrafine $La_{0.7}Ca_{0.3}MnO_z$ Powders Prepared by Mechanical Alloying. *Journal of Solid State Chemistry*. Vol. 152, (July 2000), pp. (503–510), ISSN 0022-4596.

Neumeier, J.J., Wundley, M.F., Thomson, J.D. & Heffner R.H. (1995). Substantial Pressure Effects on the Electrical Resistivity and Ferromagnetic Transition Temperature of $La_{1-x}Ca_xMnO_3$. *Physical Review B: Condensed Matter and Materials Physics*. Vol. 52, (December 1995), pp. (R7006–R7009), ISSN 1550-235x.

Sato, K., Chaichanawong, J., Abe, H., & Naito, M. (2006). Mechanochemical synthesis of $LaMnO_{3+\delta}$ fine powder assisted with water vapor. *Materials Letters*. Vol. 60, (May 2006), pp. (1399-1402), ISSN 0167-577x.

Schiffer, P., Ramirez, A.P., Bao, W. & Cheong, S-W. (1995). Low Temperature Magnetoresistance and the Magnetic Phase Diagram of $La_{1-x}A_xMnO_3$. *Physical Review Letters*. Vol. 75, (October 1995), pp. (3336–3339), ISSN 0031-9007.

Shinde, K. P., Deshpande, N.G., Eom, T., Lee, Y.P., & Pawar, S.H. (2010). Solution-combustion synthesis of $La_{0.65}Sr_{0.35}MnO_3$ and the magnetocaloric properties. *Materials Science and Engineering B.* Vol. 167, (March 2010), pp. (202-205), ISSN 0921-5107.

Shu, Q., Zhang, J., Yan, B. & Liu, J. (2009). Phase formation mechanism and kinetics in solid-state synthesis of undoped and calcium-doped lanthanum manganite. *Materials Research Bulletin*. Vol. 44, (March 2009), pp. (649-653), ISSN 0025-5408.

Tokura, Y., Urushibara, A., Moritomo, Y., Arima, T., Asamitsu, A., Kido, G. & Furukawa, N. (1994). Giant Magnetotransport Phenomena in Filling-Controlled Kondo Lattice System $La_{1-x}Sr_xMnO_3$. *Journal of the Physical Society of Japan.* Vol. 63, (September 1994), pp. (3931–3935), ISSN 1347-4073.

Uskokovic, V. & Drofenik, M. (2007). Four novel co-precipitation procedures for the synthesis of lanthanum-strontium manganites. *Materials & Design.* Vol. 18, (august 2005), pp. (667-672), ISSN 0261-3069.

Zhang, Q. & Saito, F. (2000). Mechanochemical synthesis of $LaMnO_3$ from La_2O_3 and Mn_2O_3 powders (2000). *Journal of Alloys and Compounds*. Vol. 297, (February 2000), pp. (99-103), ISSN 0925-8388.

Zhang, Q., Nakagawa, T. & Saito, F. (2000). Mechanochemical synthesis of $La_{0.7}Sr_{0.3}MnO_3$ by grinding constituent oxides. *Journal of Alloys and Compounds*. Vol. 308, (August 2000), pp. (121-125), ISSN 0925-8388.

Zhou, S. M., Zhao, S. Y., He, L. F., Guo, Y.Q. & Shi, L. (2010). Facile synthesis of Ca-doped manganite nanoparticles by a nonaqueous sol–gel method and their magnetic properties. *Materials Chemistry and Physics*. Vol. 120, (March 2010), pp. (75-78), ISSN 0254-0584.

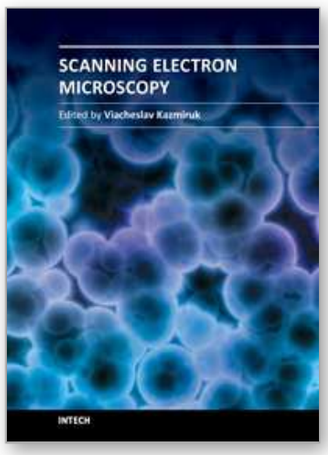

Scanning Electron Microscopy

Edited by Dr. Viacheslav Kazmiruk

ISBN 978-953-51-0092-8
Hard cover, 830 pages
Publisher InTech
Published online 09, March, 2012
Published in print edition March, 2012

Today, an individual would be hard-pressed to find any science field that does not employ methods and instruments based on the use of fine focused electron and ion beams. Well instrumented and supplemented with advanced methods and techniques, SEMs provide possibilities not only of surface imaging but quantitative measurement of object topologies, local electrophysical characteristics of semiconductor structures and performing elemental analysis. Moreover, a fine focused e-beam is widely used for the creation of micro and nanostructures. The book's approach covers both theoretical and practical issues related to scanning electron microscopy. The book has 41 chapters, divided into six sections: Instrumentation, Methodology, Biology, Medicine, Material Science, Nanostructured Materials for Electronic Industry, Thin Films, Membranes, Ceramic, Geoscience, and Mineralogy. Each chapter, written by different authors, is a complete work which presupposes that readers have some background knowledge on the subject.

InTech Europe
University Campus STeP Ri
Slavka Krautzeka 83/A
51000 Rijeka, Croatia
Phone: +385 (51) 770 447
Fax: +385 (51) 686 166
www.intechopen.com

InTech China
Unit 405, Office Block, Hotel Equatorial Shanghai
No.65, Yan An Road (West), Shanghai, 200040, China
中国上海市延安西路65号上海国际贵都大饭店办公楼405单元
Phone: +86-21-62489820
Fax: +86-21-62489821

IntechOpen